Upgrading SPHERE with the second stage AO system SAXO+: exploration of the parameter space with end-to-end numerical simulations

Charles Goulas[a], Raphaël Galicher[a], Fabrice Vidal[a], Johan Mazoyer[a], Florian Ferreira[a], Arnaud Sevin[a], Anthony Boccaletti[a], Eric Gendron[a], Clémentine Béchet[b], Michel Tallon[b], Isabelle Tallon[b], Maud Langlois[b], Magali Loupias[b], Eric Thiébaut[b], Caroline Kulcsár[c], Henri-François Raynaud[c], Nicolas Galland[c], Laura Schreiber[d], Emiliano Diolaiti[d], Isaac Bernardino Dinis[e], François Wildi[e], Gaël Chauvin[f], Julien Milli[g], David Mouillet[g], Markus Feldt[h], Markus Kasper[i], Miska Lelouarn[i], and Raffaele Gratton[j]

[a]LESIA, Observatoire de Paris, Université PSL, Université Paris-Cité, Sorbonne Université, CNRS, Meudon, France
[b]CRAL, CNRS, Université Claude Bernard Lyon 1, ENS de Lyon, France
[c]IOGS, CNRS, Laboratoire Charles Fabry, Université Paris-Saclay, France
[d]INAF, Osservatorio di Astrofisica e Scienza delle Spazio di Bologna, Italy
[e]Dept. of Astronomy, University of Geneva, Switzerland
[f]Laboratoire J.-L. Lagrange, CNRS, OCA, Université Côte d'Azur, France
[g]IPAG, CNRS, Université Grenoble Alpes, France
[h]Max-Planck-Institut für Astronomy, Germany
[i]European Southern Observatory, Germany
[j]INAF, Osservatorio Astronomico di Padova, Italy

ABSTRACT

SAXO+ is the upgrade of SAXO, the adaptive optics system used by the SPHERE instrument on ESO's Very Large Telescope. SAXO+ consists of a second stage adaptive optics downstream of the first stage, SAXO, to improve wavefront correction, achieve deeper contrast in the coronagraphic images and observe fainter and redder stars. Using the COMPASS end-to-end simulation tool, we assess the SAXO+ improved correction compared to SAXO in multiple science cases and turbulence conditions. The adaptive optics performance criterion is the starlight residual intensity in the coronagraph image : the lower the better. We show that SAXO+ improves the performance of the adaptive optics system by a factor of 10 in all simulated observing conditions. We specifically study the impact of the second stage frequenc and we conclude that a 2 kHz second stage is a reasonable trade-off between performance and technical constraints on the real-time system.

Keywords: SAXO+, multi stage AO, high-contrast imaging, numerical simulations, pyramid wavefront sensor

1. INTRODUCTION

High-contrast imaging is focused on detecting light emitted or reflected by the immediate surroundings of stars. This technique enables spectroscopic and polarimetric characterization of circumstellar disks and the atmospheres of young giant exoplanets. Such observations are challenging because stars are much brighter than their accompanying exoplanets or disks. To address this, high-contrast instruments employ a coronagraph to block on-axis starlight, allowing off-axis light from the surroundings to be detected. As coronagraphs are designed for an aberration-free wavefront, ground-based high-contrast instruments are supported by an extreme adaptive optics (AO) system. State-of-the-art exoplanet imagers include GPI at Gemini South (1), Clio2/MagAO at

Further author information: charles.goulas@obspm.fr

Adaptive Optics Systems IX, edited by Kathryn J. Jackson, Dirk Schmidt, Elise Vernet,
Proc. of SPIE Vol. 13097, 1309769 · © 2024 SPIE · 0277-786X
doi: 10.1117/12.3018709

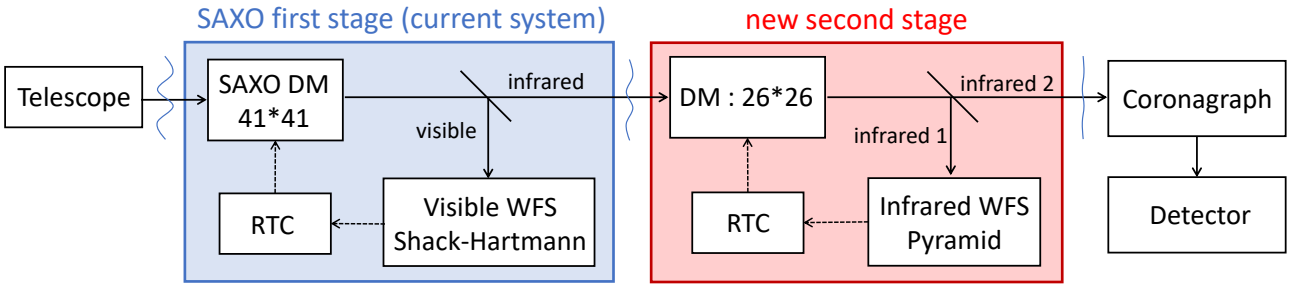

Figure 1. Current design of SAXO+. The first stage maximum frequency is 1.38 kHz, and the second stage maximum frequency is 3 kHz.

the *Magellan* telescope (2; 3), SCExAO at Subaru (4), and SPHERE at VLT (5). GPI and MagAO are being upgraded to GPI 2.0 (6) and MagAO-X (7), respectively.

Since 2014, SPHERE has been observing exoplanetary systems at the VLT. Its AO system, SAXO, features a 40x40 Shack-Hartmann wavefront sensor (WFS) operating in visible light, a 41x41 high-order deformable mirror (HODM), and a fast tip-tilt mirror, achieving a loop frequency at 1.38 kHz under high flux conditions. SAXO provides a corrected beam to three coronagraph instruments, IRDIS (8), IFS (9), and ZIMPOL (10). The starlight intensity (normalized by the maximum of the non-coronagraph image) in the raw images of SPHERE reaches 10^{-4} at 300 mas before post-processing techniques (11).

SPHERE's performance is limited by uncorrected aberrations, which may arise from AO residual turbulence or optical aberrations of the telescope and the instrument. SAXO+ (12) is a technological development of SAXO, currently in the design phase. It is part of the roadmap for the ESO instrument PCS/ELT as a demonstrator of a two-stage AO system. SAXO+ aims to observe fainter and redder stars, and to detect more exoplanets, particularly those closer to their host stars, between 100 and 300 mas. One constraint is to preserve SAXO as it is. Therefore, SAXO+ upgrade consists of adding a second stage in cascade (this stage can be bypassed to use SAXO as it is in 2024). SAXO+ will address the current limitations of SAXO, specifically the AO temporal error and WFS sensitivity. To achieve these goals, SAXO+ includes a second-stage AO, positioned downstream of the existing SAXO stage, as described in Fig. 1. The wavefront sensing will be done in near-infrared with a pyramid WFS (13, PWFS), more sensitive than the SWFS. The first stage, in blue, is the current SAXO system. The second stage, in red, will run faster, up to 3 kHz, to address the temporal error of the first stage. This meets the science case of observing redder targets. In this study, the two loops are independent, with two separate controllers, one for each stage (see section 2.4).

In this paper we present the main results of our SAXO+ numerical simulations. The explored parameter space includes key system parameters (first and second stage frequencies, first stage gain), observing conditions (seeing and coherence time of turbulence), and science cases (magnitudes in G and J band). The conclusions will contribute to SAXO+ in terms of design choice and system trade-offs. A more detailed study and analysis of our simulation campaign is available in Goulas et al 2024 (14).

2. SIMULATION FRAMEWORK

2.1 Simulation tool

We numerically simulate the atmospheric turbulence, the SAXO+ system, and the perfect coronagraph images of an on-axis point source using COMPASS, an end-to-end AO simulation tool (15). The parameters of the simulations (hardware, software, turbulence) were set using knowledge on the current system (SAXO, VLT atmosphere conditions) and on the scientific requirements (12). All parameters are summarized in Table 1 and Table 2. The explored parameter space consists in 3276 combinations of the following parameters : seeing, coherence time of turbulence, science case, first stage gain, first and second stage frequencies. Their possible values are indicated in the tables.

In Sect. 2.2, we detail the science cases identified by the SAXO+ consortium (Table 2). In Sect. 2.3, we describe the numerical simulations of the atmosphere turbulence. In Sect. 2.4, we give the assumptions we make

Table 1. Simulation parameters. The asterisk indicates the variable parameters of this study. The entries without an asterisk are fixed parameters.

Turbulence	profile	ESO 35 layer median
	outer scale	$L_0 = 25$ m
	seeing*	$s = 0.5, 0.8, 1.2$ arcsec
	coherence time*	$\tau_0 = 1, 3, 5, 7$ ms
Telescope	diameter	$D = 8$ m
	entrance pupil	VLT pupil with spiders
Shack-Hartmann WFS	wavelength	$\lambda_{\mathrm{WFS}} = 700$ nm
	subapertures	40×40
	readout noise	0.1 electrons/pixel
First stage DM	geometry	41×41 + tip-tilt mirror
	modal basis	800 KL modes
First stage control	reconstruction matrix	least squares method
	command law	integrator + scalar gain
	total delay	2.15 ms
	loop gain*	$g_1 = 0, 0.01, 0.05, 0.1, 0.2, 0.3, 0.5$
Pyramid WFS	wavelength	$\lambda_{\mathrm{WFS}} = 1.2$ µm
	subapertures	50×50
	readout noise	0.8 electrons/pixel
	modulation radius	$3\ \lambda_{\mathrm{WFS}}/D$
Second stage DM	geometry	26×26
	modal basis	400 KL modes
Second stage control	reconstruction matrix	least squares method
	command law	modal integrator
	optical gain compensation	CLOSE algorithm
	total delay	2 sampling frames
Image formation	type of coronagraph	perfect
	wavelength	$\lambda = 1.67$ µm
	exposure time	3 s

about several hardware and software subsystems of SAXO+. In Sect. 2.5 we define the normalized intensity that we use as a metric to probe the performance in this paper.

2.2 Science cases

The SAXO+ consortium defined 8 science cases, given in Table 2 (16). For each case, the science target is also the AO guide star and we provide the G and J magnitudes, as it better captures the spectral range we are dealing with in SAXO and SAXO+. We deduce the photon flux on the SH WFS from the G magnitude m_G and the photon flux on the PWFS from the J magnitude m_J. The brightest target is "bright-1", with $m_G = 5.5$ and $m_J = 5.2$. The magnitudes at the two bands increase until the faintest case "red-5". As suggested by their name, the 5 faintest targets are also red stars, with $m_G - m_J = 2.4$ for the "red-1" case and up to $m_G - m_J = 4.3$ for "red-5". For the red cases, the photon flux on the SH WFS is lower than the photon flux on the PWFS. The last two columns show the frequencies of each stage that we test in this paper. For the brightest stars, the photon flux level is high enough to run the system at the maximum speed. As the number of photons on the WFS decreases, we slow down the first or second stage to ensure there is at least 1 photo-electron per frame and per subaperture for the SH or per pixel for the PWFS.

Table 2. Science cases and simulated frequencies.

Science case	G mag	J mag	SH flux [ph-e/subap/ms]	pyramid flux [ph-e/pixel/ms]	simulated frequencies	
					1st stage [Hz]	2nd stage [Hz]
bright-1	5.5	5.2	411	146	500, 1000	1000, 2000, 3000
bright-2	7.6	7.2	59.3	23.1		
bright-3	9.6	7.8	9.41	13.3	250, 500, 1000	
red-1	11.9	8.5	1.13	6.98	50, 250, 500	
red-2	12.8	10.1	0.492	1.60		
red-3	14.5	10.1	0.130	1.60	50, 250	
red-4	15.3	11.4	0.0492	0.483		500, 1000, 2000
red-5	16.8	12.5	0.0124	0.175	10, 50, 250	100, 250, 500

2.3 Turbulence

The simulation of the atmosphere is based on the ESO 35 layer "median" profile for which we call v_{median} the effective wind speed (17). Three seeing conditions are simulated: a good seeing of 0.5", an average seeing of 0.8" and a poor seeing of 1.2". We simulate four values of coherence time : 1, 3, 5 and 7 ms. We recall that the median coherence time at Paranal is 4.5 ms and that (18) showed that the wind-driven halo dominates in the raw images of SPHERE when the coherence time of the atmosphere is below 3 ms. To simulate a specific coherence time τ_0, we compute the effective windspeed $v = 0.314\, r_0/\tau_0$, where r_0 is the Fried parameter. We then multiply the windspeed of each layer of the ESO 35 layer profile by v/v_{median}.

2.4 AO system

2.4.1 WFS

In the current SAXO system, the SH WFS is equipped with a square spatial filter in a focal plane to improve aliasing rejection. The field of view can be 0.82", 0.89", 1.07" wide or the full field view, which is selected by the telescope operator depending on the seeing (19). In the simulations, we chose the 0.82" diameter for 0.5" seeing, the 0.89" diameter for 0.8" seeing and the open position for 1.2" seeing, which are the typical operating choices. To measure the position of the spots on the SH WFS, the current system implements the thresholded/weighted center of gravity (19). We use the same algorithm in the simulations.

The Pyramid WFS is well known for its dependency to the properties of the incoming wavefront (in particular sensitivity and linearity, see 20). We decide to use the recently developed 'full pixel method' (21; 22) as this method allows a non destructive phase information on the pixels measurements while still working on the slopes domain only (no phase reconstruction). The pyramid measurement vector contains the signal of each valid pixel, normalized by the mean of the valid pixels. The valid pixels on the pyramid detector include every pixel which at least 0.1 % of the surface is inside the pupil. The modulation radius of the PWFS is set to 3 λ_{WFS}/D.

The PWFS wavelength is 1.2 µm, according to the system design choice. As the science cases of SAXO+ are mostly in H band and the SH WFS uses visible photons, the Y and J bands are dedicated to the PWFS. Recent study suggests that, unlike the SH, it is a wise choice to slightly oversample the pyramid subapertures geometry compared to the DM actuators pattern across the pupil (23). Furthermore, in SAXO+ the second stage DM has less actuators than the first stage DM and – although this is not part of this study – it is still considered by the project to use the PWFS to control the first stage DM at a later point. As such, we decide to simulate a 50 × 50 sampling to eventually accommodate for the control of the first stage DM if required (41 × 41 actuators).

The reference slopes of the SH WFS and the reference measurement vector of the PWFS are defined by a flat wavefront (no aberration) and no non-common path aberrations (NCPA) are taken into account.

2.4.2 Deformable mirror

For the first stage we simulate the SAXO deformable mirror of 41 × 41 actuators (without the dead actuators) and the tip-tilt mirror. The second stage DM is a 28 × 28 actuators. The choice of the number of actuators results from a trade-off between technical requirements (update rate, stroke), cost and market supply. The pupil

is sized to 26×26 actuators, because the optical aperture recommended by Boston Micromachines does not include the actuators at the edge, which are not fully controllable. The optical stroke is 11 µm.

For each of these deformable mirrors, we compute simplified Karhunen-Loève (KL) modes, as described by (24). We call $\boldsymbol{B}_1$ the modal basis matrix of the first stage DM and $\boldsymbol{B}_2$ the modal basis matrix of the second stage DM. The columns of $\boldsymbol{B}_1$ and $\boldsymbol{B}_2$ contain the modes of the basis expressed in the actuator space. The highest order modes are filtered by truncation. We use 800 modes on the first stage and 400 modes on the second stage (60% and 75% of the total number of actuators, respectively).

2.4.3 Command matrices

The modal interaction matrices $\boldsymbol{D}_1$ and $\boldsymbol{D}_2$ are calibrated without photon or detector noise, under infinite flux conditions. $\boldsymbol{D}_1$ contains, in column, the slopes vector of the SH WFS measured by pushing each mode of $\boldsymbol{B}_1$ one after the other with 1 nm RMS amplitude. Similarly, $\boldsymbol{D}_2$ contains, in column, the measurement vector of the PWFS obtained by pushing on each mode of $\boldsymbol{B}_2$ (one after the other with a 1 nm RMS amplitude). The same pyramid modulation is applied during the interaction matrix calibration procedure and while closing the loop.

The modal command matrices $\boldsymbol{R}_1$ and $\boldsymbol{R}_2$ are the generalized inverse of the modal interaction matrices $\boldsymbol{D}_1$ and $\boldsymbol{D}_2$ respectively. Mathematically speaking, with $j = 1$ or 2 respectively for the first and second stage :

$$\boldsymbol{R}_j = (\boldsymbol{D}_j^\intercal \boldsymbol{D}_j)^{-1} \boldsymbol{D}_j^\intercal \tag{1}$$

2.4.4 Command law

For the first stage, the command law is a temporal integrator with a scalar gain g_1, based on the following recurrence equation :

$$\boldsymbol{c}_1[i+1] = \boldsymbol{c}_1[i] - g_1 \boldsymbol{B}_1 \boldsymbol{R}_1 \boldsymbol{m}_1[i] \tag{2}$$

where $\boldsymbol{c}_1$ is the command vector containing the DM voltages of the first stage, $\boldsymbol{m}_1$ the SH slopes vector and i the iteration of the recurrence. With the gain g_1 we can handle the temporal optimization of the loop.

For the second stage, we use in addition a vector of modal gains $\boldsymbol{g}_\mathrm{m}$:

$$\boldsymbol{c}_2[i+1] = \boldsymbol{c}_2[i] - g_2 \boldsymbol{B}_2 \boldsymbol{g}_\mathrm{m} \boldsymbol{R}_2 \boldsymbol{m}_2[i] \tag{3}$$

where $\boldsymbol{c}_2$ is the command vector containing the DM voltages of the second stage and $\boldsymbol{m}_2$ is the pyramid measurement vector.

As the amplitude of a mode increases, the non-linearity of the PWFS results in a sensitivity loss. This phenomenon can be described on each mode by an optical gain between 0 and 1, that we call α_k for the mode number k. Thus, the effective gain of the loop for this mode is $g_2 \alpha_k g_k$ with g_k the k component of the modal gain vector $\boldsymbol{g}_\mathrm{m}$. The α_k optical gains describe a physical optical effect of the pyramid and they are included in the PWFS measurement $\boldsymbol{m}_2$. That is why they do not explicitly appear in Eq. 3. Several methods were developed to calibrate the optical gains and compensate for it during observations (22; 25; 26; 27; 28). In this paper, we use the CLOSE algorithm (29), a real-time optimization of the modal gains g_k. CLOSE retrieves information about the transfer function of Eq. 3 from the closed loop pyramid measurements $\boldsymbol{m}_2$. Then, with a model of the transfer function, CLOSE estimates the optimal gain of the loop and adjusts the value of g_k so that the effective gain $g_2 \alpha_k g_k$ is equal to the estimated optimal gain.

The total delay of the first stage corresponds to the value measured on the real SAXO system (1.56 ms, 18). For the second stage, we made an estimation of the time required for PWFS camera readout, RTC computational time, electronics communication and DM surface update, of about 300 µs. Thus, we set in this framework a total delay of two sampling frames.

The command laws in equations 2 and 3 are independent in this paper. In particular, the measurement of the pyramid is not used to control the first stage DM. Although an integrator with a scalar gain is a robust control scheme, this approach is quite conservative, with the exception of the CLOSE algorithm. As a two-stage AO system, SAXO+ might benefit for more ingenious control techniques. Some of them are currently studied for an implementation in the second stage RTC : linear quadratic gaussian regulator (30), disentangled cascaded AO (31), inverse problem approach (32) and data-driven control (33). However, those studies are out of the scope of this work. Our numerical simulations use a baseline controller, and the results of our parametric study will serve as a reference for future comparisons with enhanced control laws.

2.5 Criteria of performance

All images are computed using a perfect coronagraph (34) and normalized by the maximum intensity of the non coronagraphic point spread function (PSF). The normalized intensity $\eta(\boldsymbol{x})$ at a given position $\boldsymbol{x}$ in the coronagraph focal plane writes as :

$$\eta(\boldsymbol{x}) = \frac{I(\boldsymbol{x})}{\max(\mathrm{PSF})} \tag{4}$$

where $I(\boldsymbol{x})$ is the intensity of the coronagraph image before normalization. The metric we use is the azimuthal average μ of the normalized intensity η as a function of angular separation from the optical axis. At the angular separation s λ/D (s a real number), μ writes :

$$\mu(s) = \frac{1}{\mathcal{A}_s} \int_{\mathcal{A}_s} \eta(\boldsymbol{x})\, \mathrm{d}\boldsymbol{x} \tag{5}$$

where $\mathcal{A}_s$ is the ring-shaped area between the angular separation $(s-0.5)$ λ/D and $(s+0.5)$ λ/D from the star. We also compute the standard deviation of the normalized intensity over the same area.

There are several options on how to use the normalized intensity for a performance criteria. We can compare normalized intensity curves of μ with respect to the angular separation. However, for massive comparison of parameters, it is more suitable to reduce the performance criteria to one number. We define the criterion $C(s_1,\, s_2)$ as the average of the normalized intensity η between two angular separations s_1 λ/D and s_2 λ/D :

$$C(s_1,\, s_2) = \frac{1}{\mathcal{A}_{s_1,\, s_2}} \int_{\mathcal{A}_{s_1,\, s_2}} \eta(\boldsymbol{x})\, \mathrm{d}\boldsymbol{x} \tag{6}$$

where $\mathcal{A}_{s_1,\, s_2}$ is the ring-shaped area between the angular separation $(s_1 - 0.5)$ λ/D and $(s_2 + 0.5)$ λ/D . In this paper, as a baseline, we use $s_1 = 3$ and $s_2 = 5$ as one of the main science requirements of SAXO+ is to detect exoplanets the closest possible to the star (12). In several figures, the Strehl ratio (SR) is given for information (35).

3. RESULTS

3.1 Coronagraph images

Figure 2 shows the typical coronagraph images obtained with SAXO in the first row and those obtained with SAXO+ in the second row. The seeing is 0.8" and the coherence time is 3 ms. We focus on three specific science cases, bright-1, red-1, and red-4. We selected the system parameters (first and second stage frequencies and first stage gain) that give the optimal SAXO+ performance. Our performance criterion for parametric optimization is to minimize $C(3, 5)$, the average normalized intensity between 3 and 5 λ/D. The optimal parameters are written in the lower-left corner of each image in Fig. 2.

In the bright-1 case (left) with SAXO (top) in Fig. 2, the edge of the correction zone of the first stage is at 15 λ/D from the optical axis. It is set by the number of modes controlled by the SAXO system (Sect. 2.4.2). The butterfly-shaped halo is due to the AO temporal error, also known as the wind-driven halo (18). In the lower-left image, with SAXO+, the correction zone of the second stage appears inside the first one, below 10 λ/D separation. This correction zone is smaller because the second stage DM has fewer actuators and controls fewer modes than the first stage DM. The second stage, here running at 3 kHz, corrects most of the wind-driven halo left by the first AO loop. In the red-1 and red-4 cases (center and right images), SAXO does not provide effective turbulence correction at the wavelength of interest: There is no correction zone in the top images. The second stage of SAXO+ compensates by itself (gain of the first stage is 0.01) most of the turbulence, and the correction zone of DM2 is visible in the coronagraph images (bottom), improving the quality of the image with respect to SAXO case.

As the photon flux is decreasing in both WFSs from left to right in Fig. 2, the residual intensity inside the correction zones increases, and the actual performance is reduced as expected. In particular, in the red-4 case with SAXO (upper-right image), there is no correction at all, as the SR is at 0.01. Moreover, the optimal values

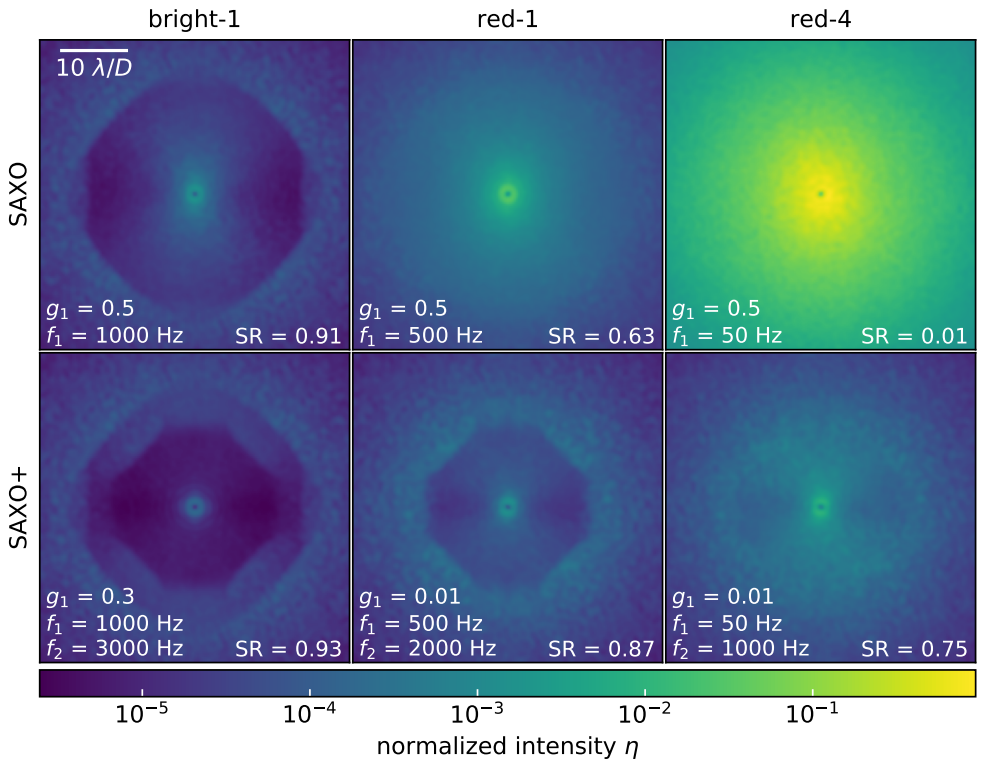

Figure 2. Coronagraph images after SAXO (first row) and SAXO+ (second row) in the science cases bright-1 (left), red-1 (center), and red-4 (right). The colorbar is the same for all image : the darker, the better. Conditions: $s = 0.8$", $\tau_0 = 3$ ms. Imaging wavelength: $\lambda = 1.67$ µm. The system parameters (gain and frequency of the first stage, respectively g_1 and f_1, and frequency of the second stage f_2) were optimized to minimize the angular distance residuals between 3 and 5 λ/D and are given in the lower-left corner of each image. The SR is in the lower-right corner.

of first stage gain, first stage frequency, and second stage frequency decrease from left to right. As expected, we needed to slow down the loops to ensure a reasonable signal-to-noise ratio on the WFS detector.

We plot in Fig. 3 the azimuthal average μ of the normalized intensity versus the angular separation (see Eq. 4). The semitransparent areas represent the azimuthal standard deviation of the normalized intensity. In our simulation, only the wind-driven halo creates asymmetry in the coronagraph images. Hence, the wider the semitransparent area in Fig. 3, the stronger the wind-driven halo.

For the bright case (blue curves in Fig. 3), from 2 to 6 λ/D, the azimuthal average μ obtained with SAXO+ is lowered by a factor of ten compared to SAXO. For instance, at 5 λ/D, we obtained a $7 \cdot 10^{-5}$ normalized intensity with SAXO+. Moreover, the standard deviation (linked to the wind-driven halo, i.e., bandwidth residuals) is also reduced, by a factor two in the SAXO+ case. At a 10 λ/D separation, we reached the edge of the second stage correction zone, with a normalized intensity of $5 \cdot 10^{-6}$ for SAXO+, improved by a factor four compared to SAXO. Further away, from 15 λ/D, the SAXO and the SAXO+ system cannot correct the turbulence, and the intensity level is dominated by the turbulence level. The correction zone cutoffs at 15 λ/D and 10 λ/D for the first and second stage are reduced compared to the theoretical DM geometry since we used only 800 and 400 modes, respectively (60% and 75% of the total number of actuators). Between 10 λ/D and 15 λ/D, we notice an intermediate correction zone, which is as expected. The zone is where the first stage can produce a correction, while the second stage cannot due to its limited number of actuators. It should be noted that if the frequency and the gain of the first stage are the same in the SAXO and the SAXO+ simulations, we find the SAXO and SAXO+ curves superimposed in Fig. 3 in this intermediate correction zone. In our case the curves are not perfectly superimposed due to differently tuned AO parameters. The gain of the first stage and the frequencies of both stages are optimized for each curve to reach the best performance between 3 λ/D and 5 λ/D. Improving the performance in this region comes with a loss of performance between 10 and 15 λ/D.

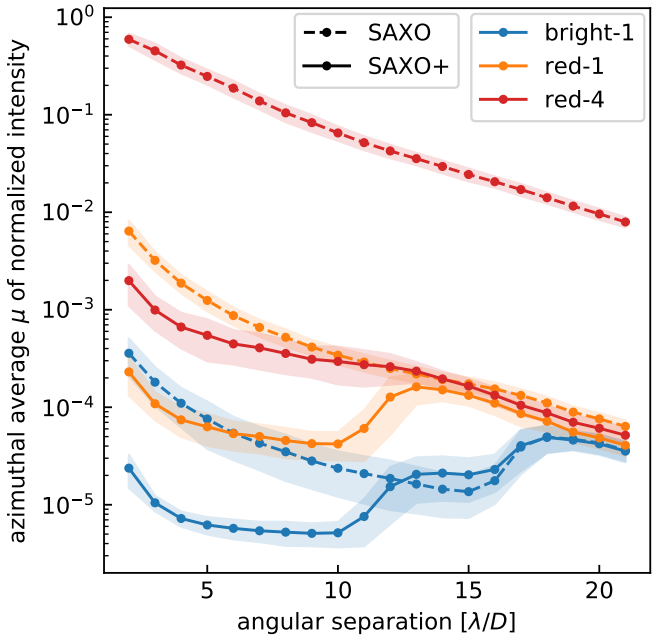

Figure 3. Azimuthal average μ of the normalized intensity of Fig. 2 images. The semitransparent areas represent the standard deviation of the normalized intensity. Conditions: $s = 0.8$", $\tau_0 = 3$ ms. Imaging wavelength: $\lambda = 1.67$ µm.

For the red-1 (orange) and red-4 (red) cases in Fig. 3, there is a loss of performance. This is expected because there are fewer photons on the WFS and the loops have to be slowed down. Nevertheless, SAXO+ always performs better than SAXO by a factor of ten to 100 (red-4).

3.2 Second stage frequency

The maximum frequency of the second stage is one of the major system trade-offs. In high flux conditions, a higher frequency means a lower stellar intensity in coronagraph images but harsher constraints on the real-time system (e.g., pyramid modulation mirror, RTC, electronics). In this section, we study the performance as a function of the second stage frequency. Figure 4 shows the azimuthal average μ of the normalized intensity versus the angular separation for SAXO (in blue) and for SAXO+ with various frequencies of the second stage (1 kHz in orange, 2 kHz in green, and 3 kHz in red) and four coherence times (1, 3, 5, 7 ms). The science case is bright-1, namely high flux conditions, and the seeing is 0.8".

For all cases (τ_0 and f_2) but one that we discuss below ($\tau_0 = 1$ ms and $f_2 = 1$ kHz), SAXO+ improves the coronagraph performance between 3 and 5 λ/D by a factor of ten or five. In all cases, the SAXO+ performance improves as f_2 increases. And the azimuthal average μ of the normalized intensity is always smaller at 3 kHz than at 2 kHz. The performance gain between the different operating frequencies narrows as the coherence time increases, which is expected because the bandwidth error becomes less and less dominant. Except for the shortest coherence time of 1 ms, the improvement of residual intensity when going from 2 to 3 kHz is less than 20 % between 3 and 5 λ/D. Given the constraints for 3 kHz (RTC, pyramid modulation, electronics), this improvement of performance may not be significant enough to justify an increase in the maximum second stage frequency from 2 kHz to 3 kHz.

If the second stage runs at 1 kHz and $\tau_0 = 1$ ms, SAXO+ does not improve the correction of SAXO beyond 6 λ/D, as the blue and orange curves are superimposed in Fig. 4 in the upper-left graph. This happens because the CLOSE algorithm lowers the modal gains on the highest order modes for the SAXO+ system to compensate for the low signal-to-noise ratio on the PWFS. To overcome this phenomenon, we could use a modal integrator on the first stage and increase the gain on high-order modes above 6 λ/D. Not only in this specific case but more generally, increasing the first stage gain for high-order modes above 10 λ/D (modes not corrected by the second stage) might improve the SAXO+ performance, compared to our current study. Indeed, it will decrease

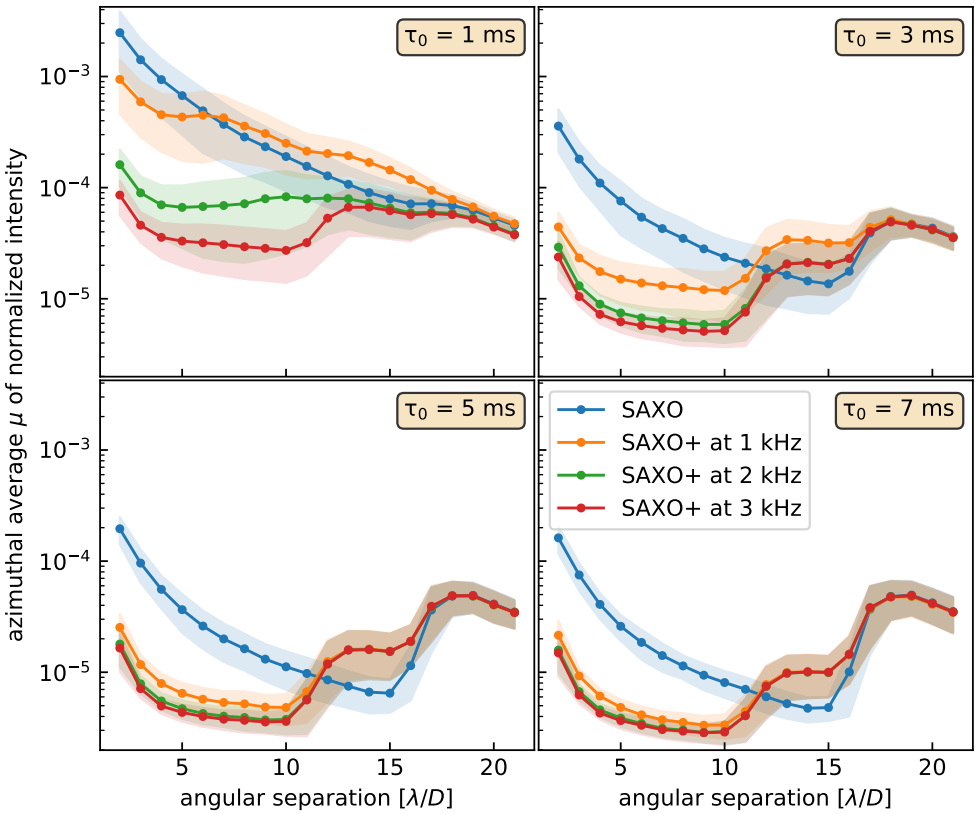

Figure 4. Azimuthal average μ of the normalized intensity for different frequencies of the second stage. Conditions: seeing = 0.8", science case = bright-1. Imaging wavelength: $\lambda = 1.67$ µm.

the normalized intensity between 10 and 15 λ/D, as the first stage gain is currently suboptimal for a SAXO-alone system. Moreover, it will improve the PSF quality at the top of the pyramid WFS and reduce aliasing effects.

3.3 Performance versus observing conditions

In Fig. 5, we compare the performance of SAXO (top) and SAXO+ (bottom) for every simulated science cases (rows) and turbulence conditions described by coherence time and seeing (columns). The values in each box of the table are the SR and the performance criterion $C(3, 5)$, which is the mean normalized intensity between 3 and 5 λ/D. The color scale is related to this performance criterion. The quality of the correction increases from red to green.

For all simulated science cases and turbulence conditions, SAXO+ improves the correction of SAXO by a factor of around 10. In terms of SR, in the bright cases SAXO and SAXO+ are both performing a high SR correction, above 0.8. While red-1 and red-2 cases are a medium SR regime for SAXO, SAXO+ increases the SR to 0.7 - 0.9 depending on the turbulence conditions. Red-3, red-4 and red-5 cases are too faint to be observable with SAXO, as the SR is between 0.01 and 0.3. However, thanks to the near-infrared WFS, this cases will be observable with SAXO+, as the SR will be mainly between 0.6 and 0.9 (except for the harshest observing conditions).

4. CONCLUSION

SAXO+ is the upgrade of SAXO, the SPHERE adaptive optics system at the Very Large Telescope. It includes a faster second-stage AO with a near-infrared pyramid WFS in cascade with the current SH SAXO system. Using end-to-end numerical simulations, we quantify the performance of the system by measuring the average coronagraph intensity between 3 and 5 λ/D. SAXO+ will enhance the detection capabilities of exoplanets by a factor 10 compared to the current system. A 2 kHz second stage seems a reasonable trade-off between

SAXO

	1 ms 0.5 "	1 ms 0.8 "	1 ms 1.2 "	3 ms 0.5 "	3 ms 0.8 "	3 ms 1.2 "	5 ms 0.5 "	5 ms 0.8 "	5 ms 1.2 "	7 ms 0.5 "	7 ms 0.8 "	7 ms 1.2 "
bright-1	0.81 $1.0\cdot10^{-3}$	0.78 $9.4\cdot10^{-4}$	0.69 $1.1\cdot10^{-3}$	0.95 $1.0\cdot10^{-4}$	0.91 $1.1\cdot10^{-4}$	0.80 $3.9\cdot10^{-4}$	0.96 $4.5\cdot10^{-5}$	0.93 $5.8\cdot10^{-5}$	0.80 $3.5\cdot10^{-4}$	0.97 $2.9\cdot10^{-5}$	0.93 $4.3\cdot10^{-5}$	0.80 $3.3\cdot10^{-4}$
bright-2	0.80 $1.1\cdot10^{-3}$	0.77 $1.0\cdot10^{-3}$	0.68 $1.2\cdot10^{-3}$	0.94 $1.5\cdot10^{-4}$	0.90 $1.6\cdot10^{-4}$	0.79 $4.5\cdot10^{-4}$	0.95 $8.8\cdot10^{-5}$	0.91 $1.0\cdot10^{-4}$	0.79 $4.1\cdot10^{-4}$	0.95 $7.1\cdot10^{-5}$	0.92 $8.8\cdot10^{-5}$	0.79 $3.7\cdot10^{-4}$
bright-3	0.74 $1.4\cdot10^{-3}$	0.70 $1.4\cdot10^{-3}$	0.61 $1.8\cdot10^{-3}$	0.89 $4.1\cdot10^{-4}$	0.85 $4.3\cdot10^{-4}$	0.74 $7.3\cdot10^{-4}$	0.91 $2.5\cdot10^{-4}$	0.88 $2.7\cdot10^{-4}$	0.76 $6.0\cdot10^{-4}$	0.93 $2.0\cdot10^{-4}$	0.89 $2.2\cdot10^{-4}$	0.77 $5.1\cdot10^{-4}$
red-1	0.40 $6.8\cdot10^{-3}$	0.27 $1.1\cdot10^{-2}$	0.22 $1.3\cdot10^{-2}$	0.67 $1.8\cdot10^{-3}$	0.63 $2.0\cdot10^{-3}$	0.54 $2.7\cdot10^{-3}$	0.78 $1.0\cdot10^{-3}$	0.74 $1.2\cdot10^{-3}$	0.62 $1.7\cdot10^{-3}$	0.81 $8.1\cdot10^{-4}$	0.77 $9.0\cdot10^{-4}$	0.65 $1.3\cdot10^{-3}$
red-2	0.21 $1.7\cdot10^{-2}$	0.08 $4.6\cdot10^{-2}$	0.06 $7.1\cdot10^{-2}$	0.54 $3.7\cdot10^{-3}$	0.43 $4.8\cdot10^{-3}$	0.37 $6.1\cdot10^{-3}$	0.66 $2.0\cdot10^{-3}$	0.59 $2.5\cdot10^{-3}$	0.50 $3.3\cdot10^{-3}$	0.72 $1.4\cdot10^{-3}$	0.65 $1.8\cdot10^{-3}$	0.53 $2.6\cdot10^{-3}$
red-3	0.03 $1.7\cdot10^{-1}$	0.01 $4.1\cdot10^{-1}$	< 0.01 $6.2\cdot10^{-1}$	0.11 $3.8\cdot10^{-2}$	0.02 $1.8\cdot10^{-1}$	0.01 $1.9\cdot10^{-1}$	0.21 $1.6\cdot10^{-2}$	0.09 $4.6\cdot10^{-2}$	0.06 $6.2\cdot10^{-2}$	0.31 $9.7\cdot10^{-3}$	0.17 $2.4\cdot10^{-2}$	0.11 $2.7\cdot10^{-2}$
red-4	0.03 $2.4\cdot10^{-1}$	0.01 $5.1\cdot10^{-1}$	< 0.01 $6.9\cdot10^{-1}$	0.05 $1.1\cdot10^{-1}$	0.01 $3.2\cdot10^{-1}$	< 0.01 $4.8\cdot10^{-1}$	0.10 $5.0\cdot10^{-2}$	0.03 $1.6\cdot10^{-1}$	0.01 $3.7\cdot10^{-1}$	0.17 $2.7\cdot10^{-2}$	0.04 $8.7\cdot10^{-2}$	0.02 $2.5\cdot10^{-1}$
red-5	0.03 $2.6\cdot10^{-1}$	0.01 $4.9\cdot10^{-1}$	< 0.01 $6.7\cdot10^{-1}$	0.03 $2.1\cdot10^{-1}$	0.01 $3.8\cdot10^{-1}$	0.01 $4.8\cdot10^{-1}$	0.03 $2.1\cdot10^{-1}$	0.01 $4.1\cdot10^{-1}$	< 0.01 $5.2\cdot10^{-1}$	0.04 $1.6\cdot10^{-1}$	0.01 $4.2\cdot10^{-1}$	0.01 $4.8\cdot10^{-1}$

SAXO+

bright-1	0.94 $5.6\cdot10^{-5}$	0.91 $3.7\cdot10^{-5}$	0.84 $5.3\cdot10^{-5}$	0.96 $6.7\cdot10^{-6}$	0.93 $7.6\cdot10^{-6}$	0.87 $1.8\cdot10^{-5}$	0.97 $3.9\cdot10^{-6}$	0.93 $5.2\cdot10^{-6}$	0.87 $1.5\cdot10^{-5}$	0.97 $2.9\cdot10^{-6}$	0.94 $4.5\cdot10^{-6}$	0.87 $1.3\cdot10^{-5}$
bright-2	0.92 $9.1\cdot10^{-5}$	0.89 $7.9\cdot10^{-5}$	0.82 $8.9\cdot10^{-5}$	0.96 $2.0\cdot10^{-5}$	0.92 $2.0\cdot10^{-5}$	0.86 $3.2\cdot10^{-5}$	0.96 $1.3\cdot10^{-5}$	0.93 $1.4\cdot10^{-5}$	0.86 $2.5\cdot10^{-5}$	0.96 $1.0\cdot10^{-5}$	0.93 $1.1\cdot10^{-5}$	0.86 $2.1\cdot10^{-5}$
bright-3	0.92 $1.2\cdot10^{-4}$	0.86 $1.2\cdot10^{-4}$	0.80 $1.5\cdot10^{-4}$	0.95 $3.7\cdot10^{-5}$	0.91 $3.8\cdot10^{-5}$	0.84 $5.1\cdot10^{-5}$	0.95 $2.5\cdot10^{-5}$	0.92 $2.6\cdot10^{-5}$	0.86 $3.8\cdot10^{-5}$	0.95 $1.9\cdot10^{-5}$	0.92 $2.1\cdot10^{-5}$	0.85 $3.2\cdot10^{-5}$
red-1	0.91 $1.7\cdot10^{-4}$	0.85 $1.8\cdot10^{-4}$	0.74 $2.6\cdot10^{-4}$	0.93 $6.3\cdot10^{-5}$	0.87 $7.8\cdot10^{-5}$	0.79 $1.2\cdot10^{-4}$	0.94 $4.4\cdot10^{-5}$	0.88 $5.4\cdot10^{-5}$	0.82 $8.1\cdot10^{-5}$	0.94 $3.5\cdot10^{-5}$	0.89 $4.4\cdot10^{-5}$	0.83 $6.5\cdot10^{-5}$
red-2	0.83 $5.4\cdot10^{-4}$	0.77 $6.0\cdot10^{-4}$	0.66 $7.9\cdot10^{-4}$	0.90 $2.1\cdot10^{-4}$	0.84 $2.3\cdot10^{-4}$	0.74 $3.2\cdot10^{-4}$	0.91 $1.3\cdot10^{-4}$	0.86 $1.5\cdot10^{-4}$	0.77 $2.1\cdot10^{-4}$	0.92 $1.0\cdot10^{-4}$	0.86 $1.2\cdot10^{-4}$	0.78 $1.7\cdot10^{-4}$
red-3	0.83 $5.5\cdot10^{-4}$	0.77 $6.0\cdot10^{-4}$	0.66 $7.9\cdot10^{-4}$	0.90 $2.1\cdot10^{-4}$	0.84 $2.3\cdot10^{-4}$	0.73 $3.3\cdot10^{-4}$	0.91 $1.3\cdot10^{-4}$	0.86 $1.5\cdot10^{-4}$	0.75 $2.4\cdot10^{-4}$	0.92 $1.0\cdot10^{-4}$	0.86 $1.2\cdot10^{-4}$	0.75 $2.0\cdot10^{-4}$
red-4	0.66 $2.0\cdot10^{-3}$	0.58 $2.3\cdot10^{-3}$	0.45 $3.1\cdot10^{-3}$	0.82 $6.0\cdot10^{-4}$	0.75 $7.0\cdot10^{-4}$	0.65 $9.0\cdot10^{-4}$	0.86 $3.7\cdot10^{-4}$	0.81 $3.9\cdot10^{-4}$	0.70 $5.6\cdot10^{-4}$	0.88 $2.7\cdot10^{-4}$	0.82 $3.1\cdot10^{-4}$	0.71 $4.3\cdot10^{-4}$
red-5	0.39 $8.3\cdot10^{-3}$	0.29 $1.1\cdot10^{-2}$	0.16 $1.8\cdot10^{-2}$	0.70 $1.6\cdot10^{-3}$	0.61 $1.9\cdot10^{-3}$	0.48 $2.8\cdot10^{-3}$	0.76 $9.9\cdot10^{-4}$	0.69 $1.1\cdot10^{-3}$	0.58 $1.6\cdot10^{-3}$	0.81 $7.2\cdot10^{-4}$	0.75 $7.8\cdot10^{-4}$	0.63 $1.0\cdot10^{-3}$

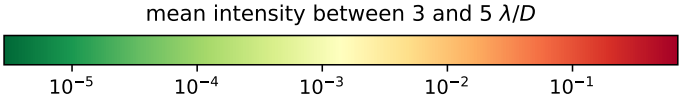

Figure 5. Strehl ratio and mean normalized intensity between 3 and 5 λ/D with respect to the science cases (rows) and the turbulence conditions (columns). Top : SAXO, bottom : SAXO+.

performance and system requirements. The full results of our parametric study are available in Goulas et al 2024 (14).

With such SAXO+ performance presented in this paper, the intensity in the raw coronagraph image will be dominated by the coronagraph diffraction pattern and the quasi-static speckles induced by NCPA. We are working on the combination of the two-stage AO with a focal plane wavefront sensor loop to correct for NCPA and reduce the coronagraph intensity below the diffraction pattern (36).

References

[1] Macintosh, B., Chilcote, J. K., Bailey, V. P., de Rosa, R., Nielsen, E., Norton, A., Poyneer, L., Wang, J., Ruffio, J.-B., Graham, J. R., Marois, C., Savransky, D., and Veran, J.-P., "The Gemini Planet Imager: looking back over five years and forward to the future," in [*Adaptive Optics Systems VI*], Close, L. M., Schreiber, L., and Schmidt, D., eds., **10703**, 107030K, International Society for Optics and Photonics, SPIE (2018).

[2] Sivanandam, S., Hinz, P. M., Heinze, A. N., Freed, M., and Breuninger, A. H., "Clio: a 3-5 micron AO planet-finding camera," in [*Ground-based and Airborne Instrumentation for Astronomy*], McLean, I. S. and Iye, M., eds., **6269**, 62690U, International Society for Optics and Photonics, SPIE (2006).

[3] Close, L. M., Gasho, V., Kopon, D., Males, J., Follette, K. B., Brutlag, K., Uomoto, A., and Hare, T., "The Magellan Telescope Adaptive Secondary AO System: a visible and mid-IR AO facility," in [*Adaptive Optics Systems II*], Ellerbroek, B. L., Hart, M., Hubin, N., and Wizinowich, P. L., eds., **7736**, 773605, International Society for Optics and Photonics, SPIE (2010).

[4] Jovanovic, N., Martinache, F., Guyon, O., Clergeon, C., Singh, G., Kudo, T., Garrel, V., Newman, K., Doughty, D., Lozi, J., Males, J., Minowa, Y., Hayano, Y., Takato, N., Morino, J., Kuhn, J., Serabyn, E., Norris, B., Tuthill, P., Schworer, G., Stewart, P., Close, L., Huby, E., Perrin, G., Lacour, S., Gauchet, L., Vievard, S., Murakami, N., Oshiyama, F., Baba, N., Matsuo, T., Nishikawa, J., Tamura, M., Lai, O., Marchis, F., Duchene, G., Kotani, T., and Woillez, J., "The subaru coronagraphic extreme adaptive optics system: Enabling high-contrast imaging on solar-system scales," *Publications of the Astronomical Society of the Pacific* **127**, 890 (sep 2015).

[5] Beuzit, J.-L., Vigan, A., Mouillet, D., Dohlen, K., Gratton, R., Boccaletti, A., Sauvage, J.-F., Schmid, H. M., Langlois, M., Petit, C., Baruffolo, A., Feldt, M., Milli, J., Wahhaj, Z., Abe, L., Anselmi, U., Antichi, J., Barette, R., Baudrand, J., Baudoz, P., Bazzon, A., Bernardi, P., Blanchard, P., Brast, R., Bruno, P., Buey, T., Carbillet, M., Carle, M., Cascone, E., Chapron, F., Charton, J., Chauvin, G., Claudi, R., Costille, A., Caprio, V. D., de Boer, J., Delboulbe, A., Desidera, S., Dominik, C., Downing, M., Dupuis, O., Fabron, C., Fantinel, D., Farisato, G., Feautrier, P., Fedrigo, E., Fusco, T., Gigan, P., Ginski, C., Girard, J., Giro, E., Gisler, D., Gluck, L., Gry, C., Henning, T., Hubin, N., Hugot, E., Incorvaia, S., Jaquet, M., Kasper, M., Lagadec, E., Lagrange, A.-M., Coroller, H. L., Mignant, D. L., Ruyet, B. L., Lessio, G., Lizon, J.-L., Llored, M., Lundin, L., Madec, F., Magnard, Y., Marteaud, M., Martinez, P., Maurel, D., Ménard, F., Mesa, D., Möller-Nilsson, O., Moulin, T., Moutou, C., Origné, A., Parisot, J., Pavlov, A., Perret, D., Pragt, J., Puget, P., Rabou, P., Ramos, J., Reess, J.-M., Rigal, F., Rochat, S., Roelfsema, R., Rousset, G., Roux, A., Saisse, M., Salasnich, B., Santambrogio, E., Scuderi, S., Segransan, D., Sevin, A., Siebenmorgen, R., Soenke, C., Stadler, E., Suarez, M., Tiphène, D., Turatto, M., Udry, S., Vakili, F., Waters, L. B. F. M., Weber, L., Wildi, F., Zins, G., and Zurlo, A., "SPHERE: the exoplanet imager for the very large telescope," *Astronomy & Astrophysics* **631**, A155 (nov 2019).

[6] Chilcote, J., Konopacky, Q., Fitzsimmons, J., Hamper, R., Macintosh, B., Marois, C., Savransky, D., Soummer, R., Véran, J.-P., Agapito, G., Aleman, A., Ammons, S. M., Bonaglia, M., Boucher, M.-A., Curliss, M., De Rosa, R. J., Do Ó, C. R., Dunn, J., Esposito, S., Filion, G., Kerley, D., Landry, J.-T., Lardiere, O., Levinstein, D., Li, D., Limbach, M. A., Madurowicz, A., Maire, J., Millar-Blanchaer, M., Nickson, B., Nielsen, E. L., Nguyen, J., Nguyen, M., Peng, D., Perera, S., Perrin, M., Por, E., Poyneer, L., Pueyo, L., Rantakyrö, F., Sands, B., Spalding, E., and Summey, K., "GPI 2.0: upgrade status of the Gemini

Planet Imager," in [*Ground-based and Airborne Instrumentation for Astronomy IX*], Evans, C. J., Bryant, J. J., and Motohara, K., eds., *Society of Photo-Optical Instrumentation Engineers (SPIE) Conference Series* **12184**, 121841T (Aug. 2022).

[7] Males, J. R., Close, L. M., Haffert, S., Long, J. D., Hedglen, A. D., Pearce, L., Weinberger, A. J., Guyon, O., Knight, J. M., McLeod, A., Kautz, M., Gorkom, K. V., Lumbres, J., Schatz, L., Rodack, A., Gasho, V., Kueny, J., and Foster, W., "MagAO-X: current status and plans for Phase II," in [*Adaptive Optics Systems VIII*], Schreiber, L., Schmidt, D., and Vernet, E., eds., **12185**, 1218509, International Society for Optics and Photonics, SPIE (2022).

[8] Dohlen, K., Langlois, M., Saisse, M., Hill, L., Origne, A., Jacquet, M., Fabron, C., Blanc, J.-C., Llored, M., Carle, M., Moutou, C., Vigan, A., Boccaletti, A., Carbillet, M., Mouillet, D., and Beuzit, J.-L., "The infra-red dual imaging and spectrograph for SPHERE: design and performance," in [*Ground-based and Airborne Instrumentation for Astronomy II*], McLean, I. S. and Casali, M. M., eds., *Society of Photo-Optical Instrumentation Engineers (SPIE) Conference Series* **7014**, 70143L (July 2008).

[9] Mesa, D., Gratton, R., Zurlo, A., Vigan, A., Claudi, R. U., Alberi, M., Antichi, J., Baruffolo, A., Beuzit, J. L., Boccaletti, A., Bonnefoy, M., Costille, A., Desidera, S., Dohlen, K., Fantinel, D., Feldt, M., Fusco, T., Giro, E., Henning, T., Kasper, M., Langlois, M., Maire, A. L., Martinez, P., Moeller-Nilsson, O., Mouillet, D., Moutou, C., Pavlov, A., Puget, P., Salasnich, B., Sauvage, J. F., Sissa, E., Turatto, M., Udry, S., Vakili, F., Waters, R., and Wildi, F., "Performance of the VLT Planet Finder SPHERE. II. Data analysis and results for IFS in laboratory," **576**, A121 (Apr. 2015).

[10] Schmid, H. M., Bazzon, A., Roelfsema, R., Mouillet, D., Milli, J., Menard, F., Gisler, D., Hunziker, S., Pragt, J., Dominik, C., Boccaletti, A., Ginski, C., Abe, L., Antoniucci, S., Avenhaus, H., Baruffolo, A., Baudoz, P., Beuzit, J. L., Carbillet, M., Chauvin, G., Claudi, R., Costille, A., Daban, J. B., de Haan, M., Desidera, S., Dohlen, K., Downing, M., Elswijk, E., Engler, N., Feldt, M., Fusco, T., Girard, J. H., Gratton, R., Hanenburg, H., Henning, T., Hubin, N., Joos, F., Kasper, M., Keller, C. U., Langlois, M., Lagadec, E., Martinez, P., Mulder, E., Pavlov, A., Podio, L., Puget, P., Quanz, S. P., Rigal, F., Salasnich, B., Sauvage, J. F., Schuil, M., Siebenmorgen, R., Sissa, E., Snik, F., Suarez, M., Thalmann, C., Turatto, M., Udry, S., van Duin, A., van Holstein, R. G., Vigan, A., and Wildi, F., "SPHERE/ZIMPOL high resolution polarimetric imager. I. System overview, PSF parameters, coronagraphy, and polarimetry," **619**, A9 (Nov. 2018).

[11] Cantalloube, F., Dohlen, K., Milli, J., Brandner, W., and Vigan, A., "Peering through SPHERE Images: A Glance at Contrast Limitations," *The Messenger* **176**, 25–31 (June 2019).

[12] Boccaletti, A., Chauvin, G., Mouillet, D., Absil, O., Allard, F., Antoniucci, S., Augereau, J. C., Barge, P., Baruffolo, A., Baudino, J. L., Baudoz, P., Beaulieu, M., Benisty, M., Beuzit, J. L., Bianco, A., Biller, B., Bonavita, B., Bonnefoy, M., Bos, S., Bouret, J. C., Brandner, W., Buchschache, N., Carry, B., Cantalloube, F., Cascone, E., Carlotti, A., Charnay, B., Chiavassa, A., Choquet, E., Clenet, Y., Crida, A., De Boer, J., De Caprio, V., Desidera, S., Desert, J. M., Delisle, J. B., Delorme, P., Dohlen, K., Doelman, D., Dominik, C., Orazi, V. D., Dougados, C., Doute, S., Fedele, D., Feldt, M., Ferreira, F., Fontanive, C., Fusco, T., Galicher, R., Garufi, A., Gendron, E., Ghedina, A., Ginski, C., Gonzalez, J. F., Gratadour, D., Gratton, R., Guillot, T., Haffert, S., Hagelberg, J., Henning, T., Huby, E., Janson, M., Kamp, I., Keller, C., Kenworthy, M., Kervella, P., Kral, Q., Kuhn, J., Lagadec, E., Laibe, G., Langlois, M., Lagrange, A. M., Launhardt, R., Leboulleux, L., Le Coroller, H., Li Causi, G., Loupias, M., Maire, A. L., Marleau, G., Martinache, F., Martinez, P., Mary, D., Mattioli, M., Mazoyer, J., Meheut, H., Menard, F., Mesa, D., Meunier, N., Miguel, Y., Milli, J., Min, M., Molliere, P., Mordasini, C., Moretto, G., Mugnier, L., Muro Arena, G., Nardetto, N., Diaye, M. N., Nesvadba, N., Pedichini, F., Pinilla, P., Por, E., Potier, A., Quanz, S., Rameau, J., Roelfsema, R., Rouan, D., Rigliaco, E., Salasnich, B., Samland, M., Sauvage, J. F., Schmid, H. M., Segransan, D., Snellen, I., Snik, F., Soulez, F., Stadler, E., Stam, D., Tallon, M., Thebault, P., Thiebaut, E., Tschudi, C., Udry, S., van Holstein, R., Vernazza, P., Vidal, F., Vigan, A., Waters, R., Wildi, F., Willson, M., Zanutta, A., Zavagno, A., and Zurlo, A., "SPHERE+: Imaging young Jupiters down to the snowline," *arXiv e-prints* , arXiv:2003.05714 (Mar. 2020).

[13] Ragazzoni, R., "Pupil plane wavefront sensing with an oscillating prism," *Journal of Modern Optics* **43**, 289–293 (Feb. 1996).

[14] Goulas, C., Galicher, R., Vidal, F., Mazoyer, J., Ferreira, F., Sevin, A., Boccaletti, A., Gendron, E., Béchet, C., Tallon, M., Langlois, M., Kulcsár, C., Raynaud, H.-F., Galland, N., Schreiber, L., Dinis, I. B., Wildi, F., Chauvin, G., and Milli, J., "Numerical simulations for the saxo+ upgrade: Performance analysis of the adaptive optics system," (2024).

[15] Gratadour, D., Ferreira, F., Sevin, A., Doucet, N., Clénet, Y., Gendron, E., Lainé, M., Vidal, F., Brulé, J., Puech, M., Vérinaud, C., and Carlotti, A., "COMPASS: status update and long term development plan," in [*Adaptive Optics Systems V*], Marchetti, E., Close, L. M., and Véran, J.-P., eds., **9909**, 990971, International Society for Optics and Photonics, SPIE (2016).

[16] Schreiber, L., Langlois, M., Jolissaint, L., Diolaiti, E., Béchet, C., Cortecchia, F., Feldt, M., Ferreira, F., Raphael, G., Charles, G., Caroline, K., Lombini, M., Magali, L., Johan, M., Mamadou, N., Raynaud, H. F., Stadler, E., Tallon, M., Tallon-Bosc, I., Thiébaut, E., Vidal, F., Boccaletti, A., Chauvin, G., Gratton, R., Milli, J., Mouillet, D., and Wildi, F., "An analytical approach to model the second-stage Adaptive Optics correction for SPHERE," in [*Adaptive Optics for Extremely Large Telescopes 7th Edition*], ONERA (June 2023).

[17] Vidal, F., Rozel, M., Deo, V., Ferreira, F., Sevin, A., Gendron, E., Clénet, Y., Gratadour, D., Rousset, G., and Davies, R., "Analysis the MICADO-MAORY SCAO performance," in [*Proceedings of the AO4ELT6 conference*], 401–PG7Z–251 (Nov. 2019).

[18] Cantalloube, F., Farley, O. J. D., Milli, J., Bharmal, N., Brandner, W., Correia, C., Dohlen, K., Henning, T., Osborn, J., Por, E., Valles, M. S., and Vigan, A., "Wind-driven halo in high-contrast images," *Astronomy & Astrophysics* **638**, A98 (jun 2020).

[19] Sauvage, J.-F., Fusco, T., Petit, C., Mouillet, D., Dohlen, K., Costille, A., Beuzit, J.-L., Baruffolo, A., Kasper, M. E., Valles, M. S., Downing, M., Feautrier, P., Mugnier, L., and Baudoz, P., "Wave-front sensor strategies for SPHERE: first on-sky results and future improvements," in [*Adaptive Optics Systems IV*], Marchetti, E., Close, L. M., and Véran, J.-P., eds., **9148**, 914847, International Society for Optics and Photonics, SPIE (2014).

[20] Vérinaud, C., "On the nature of the measurements provided by a pyramid wave-front sensor," *Optics Communications* **233**, 27–38 (Mar. 2004).

[21] Clergeon, C., *Etude d'un analyseur de surface d'onde haute sensibilité pour l'optique adaptative extrême*, theses, Observatoire de Paris (Apr. 2014).

[22] Deo, V., Gendron, É., Rousset, G., Vidal, F., Buey, T., and Cohen, M., "Assessing and mitigating alignment defects of the pyramid wavefront sensor: a translation insensitive control method," **619**, A56 (Nov. 2018).

[23] Vidal, F., Ferreira, F., Déo, V., Sevin, A., Gendron, E., Clénet, Y., Durand, S., Gratadour, D., Doucet, N., Rousset, G., and Davies, R., "End-to-End simulations for the MICADO-MAORY SCAO mode," in [*Proceedings of Adaptive Optics for Extremely Large Telescopes (AO4ELT5*], 43 (Apr. 2018).

[24] Bertrou-Cantou, A., Gendron, E., Rousset, G., Deo, V., Ferreira, F., Sevin, A., and Vidal, F., "Confusion in differential piston measurement with the pyramid wavefront sensor," **658**, A49 (Feb. 2022).

[25] Korkiakoski, V., Vérinaud, C., and Louarn, M. L., "Improving the performance of a pyramid wavefront sensor with modal sensitivity compensation," *Appl. Opt.* **47**, 79–87 (Jan 2008).

[26] Esposito, S., Puglisi, A., Pinna, E., Agapito, G., Quirós-Pacheco, F., Véran, J. P., and Herriot, G., "On-sky correction of non-common path aberration with the pyramid wavefront sensor," **636**, A88 (Apr. 2020).

[27] Chambouleyron, V., Fauvarque, O., Sauvage, J. F., Neichel, B., and Fusco, T., "Focal-plane-assisted pyramid wavefront sensor: Enabling frame-by-frame optical gain tracking," **649**, A70 (May 2021).

[28] Agapito, G., Pinna, E., Esposito, S., Heritier, C. T., and Oberti, S., "Non-modulated pyramid wavefront sensor. Use in sensing and correcting atmospheric turbulence," **677**, A168 (Sept. 2023).

[29] Deo, V., Gendron, É., Vidal, F., Rozel, M., Sevin, A., Ferreira, F., Gratadour, D., Galland, N., and Rousset, G., "A correlation-locking adaptive filtering technique for minimum variance integral control in adaptive optics," *Astronomy & Astrophysics* **650**, A41 (June 2021).

[30] Sivo, G., Kulcsár, C., Conan, J.-M., Raynaud, H.-F., Gendron, É., Basden, A., Vidal, F., Morris, T., Meimon, S., Petit, C., Gratadour, D., Martin, O., Hubert, Z., Sevin, A., Perret, D., Chemla, F., Rousset, G., Dipper, N., Talbot, G., Younger, E., Myers, R., Henry, D., Todd, S., Atkinson, D., Dickson, C., and Longmore, A., "First on-sky SCAO validation of full LQG control with vibration mitigation on the CANARY pathfinder," *Optics Express* **22**, 23565 (Sept. 2014).

[31] Galland, N., Raynaud, H. F., Kasper, M., Goulas, C., Béchet, C., Ferreira, F., Tallon, M., Vidal, F., Langlois, M., Boccaletti, A., Chauvin, G., Diolaiti, E., Gratton, R., Loupias, M., Milli, J., Wildi, F., and Kulcsar, C., "Disentangled cascade adaptive optics for the SPHERE instrument forthcoming upgrade," in [*Adaptive Optics for Extremely Large Telescopes (AO4ELT7)*], 74 (June 2023).

[32] Béchet, C., Tallon, M., Thiébaut, E., Tallon-Bosc, I., Langlois, M., Loupias, M., Kulcsar, C., Raynaud, H. F., Galland, N., Dinis, I., Goulas, C., Vidal, F., Milli, J., Mazoyer, J., Galicher, R., Schreiber, L., Feldt, M., Boccaletti, A., Diolaiti, E., Chauvin, G., Wildi, F., and Gratton, R., "Inverse problem approach for SPHERE+ adaptive optics control," in [*Adaptive Optics for Extremely Large Telescopes (AO4ELT7)*], 47 (June 2023).

[33] Dinis, I., "Data-driven control and two stages AO system for SPHERE instrument," (2022).

[34] Goulas, C., Vidal, F., Galicher, R., Mazoyer, J., Ferreira, F., Sevin, A., Boccaletti, A., Gendron, É., Béchet, C., Tallon, M., Langlois, M., Kulcsár, C., Raynaud, H.-F., Galland, N., Schreiber, L., Chauvin, G., and Milli, J., "SAXO+ upgrade : second stage AO system end-to-end numerical simulations," *arXiv e-prints* , arXiv:2310.15765 (Oct. 2023).

[35] Mahajan, V. N., "Strehl ratio for primary aberrations in terms of their aberration variance," *Journal of the Optical Society of America (1917-1983)* **73**, 860 (Jan. 1983).

[36] Potier, A., Mazoyer, J., Wahhaj, Z., Baudoz, P., Chauvin, G., Galicher, R., and Ruane, G., "Increasing the raw contrast of VLT/SPHERE with the dark hole technique. II. On-sky wavefront correction and coherent differential imaging," **665**, A136 (Sept. 2022).